

A High Incidence of Central Star Formation Inferred from the Color Gradients of Galaxies at $z > 4$

BINGCHENG JIN (金秉诚) ^{1,2} LUIS C. HO ^{1,2} AND WEN SUN (孙文) ^{1,2}

¹*Kavli Institute for Astronomy and Astrophysics, Peking University, Beijing 100871, China*

²*Department of Astronomy, School of Physics, Peking University, Beijing 100871, China*

ABSTRACT

We study the rest-frame ultraviolet-optical color gradients of 669 galaxies at $4 < z < 8$ by characterizing the wavelength dependence of their structural parameters derived from simultaneously fitting the seven-band NIRC*am* images acquired with the James Webb Space Telescope. Distinct from trends observed at lower redshifts, where most galaxies exhibit negative color gradients whereby galaxy centers are redder than their outskirts, in high-redshift galaxies positive color gradients match or even outnumber negative color gradients. The color gradients principally reflect radial variations in stellar population instead of dust reddening or contamination from active galactic nuclei. The sign and magnitude of the color profile depend systematically on the global properties of the galaxy: positive color gradients, characteristic of centrally concentrated star formation or outside-in growth, preferentially inhabit galaxies of lower stellar mass, smaller size, and bluer spectral energy distribution.

Keywords: Early universe (435); Galaxy formation (595); Galaxy evolution (594); High-redshift galaxies (734)

1. INTRODUCTION

The structure and morphology of galaxies, and how these properties change with time, reflect how galaxies evolve through their varied accretion and merger histories (White & Frenk 1991; Steinmetz & Navarro 2002). Observations across a wide range of redshifts increasingly suggest that galaxies experience “inside-out” growth (e.g., van Dokkum et al. 2010; Pérez et al. 2013; Marian et al. 2018; Frankel et al. 2019). After an early phase in which a central bulge rapidly builds up, an extended disk gradually accumulates through accretion and minor mergers. This scenario is supported by a variety of observational clues, ranging from spatially resolved, coherent star formation (Nelson et al. 2016; Matharu et al. 2024), evidence of inside-out quenching (Tacchella et al. 2015; Abdurro’uf & Akiyama 2018), and the redshift evolution of galaxy size (van der Wel et al. 2014b; Suess et al. 2019).

Among the many possible empirical indicators that can be used to diagnose the complex evolutionary pathway of a galaxy, one of the most direct and arguably

simplest approaches is through the measurement of its radial color gradient. The radial gradient of color in a galaxy reflects the spatial variation of stellar age, metallicity, and dust extinction. However, the interplay among these factors is complex and varies strongly with galaxy type, environment, and cosmic epoch. For example, the color gradients of nearby early-type galaxies largely reflect radial variations in metallicity induced by their metal-rich centers (Vader et al. 1988; Marian et al. 2018), while in late-type galaxies negative color gradients arise from younger stellar populations in their outer region (Ryder & Dopita 1994). Systematic studies of galaxies in the local Universe (e.g., Muñoz-Mateos et al. 2007; Kelvin et al. 2012) find a preponderance of negative color gradients—color profiles that are redder in the center and bluer in the outskirts—with a propensity for stronger negative color gradients in galaxies of late-type or lower Sérsic (1968) indices (Kennedy et al. 2015). Negative color gradients, albeit of weaker strength and larger scatter, continue to be seen out to galaxies at $z \approx 1 - 2$ (Suess et al. 2019; Miller et al. 2023; van der Wel et al. 2024).

Dust attenuation presents a major practical challenge to the interpretation of observed color gradients, for the effects of reddening can be confused with intrinsic variations in stellar population (Graham & Worley 2008;

Miller et al. 2022; Zhang et al. 2023). Wang et al. (2017) found that the radial color profiles of $0.4 < z < 1.4$ star-forming main sequence galaxies are affected more by dust than stellar population variations. Similarly, the larger galaxy sizes measured in the rest-frame ultraviolet (UV) compared to the optical, often interpreted as evidence that the central regions of galaxies have older stellar populations (e.g., Mosleh et al. 2012) may arise, instead, from heavier dust attenuation in the centers of massive galaxies (Nedkova et al. 2024b). However, the role of dust attenuation is less clear at high redshifts. Dust may be less of a concern at $z \gtrsim 4$ (e.g., Fudamoto et al. 2020; Looser et al. 2024; Mitsuhashi et al. 2024) given the limited time for metal enrichment and the lower dust-to-gas ratios expected, especially for low-mass systems (Li et al. 2019).

The James Webb Space Telescope (JWST) ushers in an unprecedented opportunity to resolve fainter, redder, and more distant galaxies, especially in their rest-frame optical and near-infrared wavelengths (e.g., Abdurro’uf et al. 2023; Giménez-Arteaga et al. 2023; Matharu et al. 2023). Inside-out growth may have begun very early, judging by the core-disk structure of the galaxy at $z = 7.43$ reported by Baker et al. (2024). Studying the size evolution of galaxies at $0.5 < z < 5$, Ji et al. (2024) suggest that negative color gradients have already been established in massive quiescent systems at $z > 3$. By contrast, Ono et al. (2024) find that galaxies at $z > 4$ have almost identical effective radii in the rest-frame UV and optical, indicating little evidence for color gradients, which, if anything, are more likely positive instead of negative (Morishita et al. 2024). At even higher redshifts, no trends between morphology and colors have been detected in galaxies at $z = 7-12$ (Yang et al. 2022; Treu et al. 2023). These seemingly contradictory results from JWST call for a more concerted study of galaxy color gradients at high redshift. It remains to be seen to what extent robust color gradients have already been established at these early epochs, and, if so, what the main driver behind them is and what galaxy properties correlate with them.

We take advantage of JWST images taken with the Near Infrared Camera (NIRCam; Rieke et al. 2023) from the Cosmic Evolution Early Release Science (CEERS; Finkelstein et al. 2023) program to conduct a systematic study of the color gradients of 669 galaxies at $z > 4$ and investigate their dependence on galaxy properties. The CEERS survey is designed to study the processes of galaxy assembly and the abundance and physical nature of galaxies in the early Universe. Although broadly similar topics have been studied recently with data from JWST, as mentioned above, our approach differs in sev-

eral key aspects. Measuring structural parameters with robust uncertainties for high-redshift galaxies remains challenging, notwithstanding the impressive data from JWST. Accurate parametric fits of the galaxies are obtained by simultaneously modeling the seven-band NIRCam images. Detailed mock experiments are performed to account for systematic uncertainties in the final error budget. Section 2 describes the observational material and sample definition. Section 3 introduces our image analysis technique and methodology to quantify color gradient. Results are given in Section 4, their implications are discussed in Section 5, and Section 6 summarizes the main findings. We assume a cosmology with $H_0 = 67.7 \text{ km s}^{-1} \text{ Mpc}^{-1}$, $\Omega_m = 0.307$, and $\Omega_\Lambda = 0.693$ (Planck Collaboration et al. 2020). All magnitudes are expressed in the absolute bolometric system of Oke & Gunn (1983).

2. DATA AND SAMPLE DEFINITION

We use the NIRCam imaging data from the CEERS program, which covers $\sim 100 \text{ arcmin}^2$ with three short-wavelength bands (F115W, F150W, F200W) and four long-wavelength bands (F277W, F356W, F410M, F444W). The mosaics of the 10 pointings overlap with the CANDELS Extended Groth Strip (EGS) region, one of the most well-studied fields (Koekemoer et al. 2011) in the era of the Hubble Space Telescope (HST). The CEERS team has published their data release after two epochs of observations (Finkelstein et al. 2023). We directly download the latest version of the reduced data from the CEERS website¹. The data reduction process is discussed thoroughly in Bagley et al. (2023), and the reduction scripts are available on GitHub². Although various approaches have been adopted to reduce these data (e.g., Morishita et al. 2024; Zhuang et al. 2024), each tailored for a particular purpose, the structural parameter measurements are mostly consistent with each other (e.g., see Figure 9 in Sun et al. 2024a).

The point-spread function (PSF) is crucial for determining accurate structural parameters, especially for compact, high-redshift galaxies. For the four pointings of the first epoch of the CEERS observations (CEERS1, CEERS2, CEERS3, and CEERS6), Sun et al. (2024a, see their Section 3.2 and Appendix A) constructed a PSF model for each band by stacking isolated, unsaturated point-like sources that have the spectral energy distribution (SED) of stars. Because of the relatively small number of objects available, they did not produce a separate PSF for each pointing, but, instead, for each

¹ <https://ceers.github.io/releases.html>

² <https://github.com/ceers/ceers-nircam>

filter, the objects in all pointings were combined to create a master, stacked PSF of high signal-to-noise ratio. PSF variations across different pointings of the same epoch should be small because the pointings were taken close in time and utilize the same dither pattern (Bagley et al. 2023). A 81×81 pixel cutout was extracted for each object, and all the cutouts are 4 times oversampled to align their centers after removing the background. The final PSF was constructed by mean-combining the individual stars and resampling the oversampled images to their original resolution. For the pointings from the first epoch, we directly adopt the PSF library created by Sun et al. (2024a), and we exactly follow their procedure to create the PSFs for the remaining six pointings from the second epoch observations.

To prepare for the image analysis, we carry out the following steps to extract sources from the CEERS mosaics. We apply `Photutils` (Bradley et al. 2024) to perform 1σ source detection on an image of high signal-to-noise ratio created by stacking the images of all the long-wavelength bands (F277W, F356W, F410M, F444W), weighted by their error. Many high-redshift galaxies are faint. If they are outshined by bright neighboring sources, we use the `deblend_sources` function to separate them. The catalog is then constructed with the deblended segmentation map. We crossmatch our source catalog with the CANDELS photometric redshift catalog (Stefanon et al. 2017), whose detection was based on the HST F160W band, with a 5σ limiting magnitude of 27.6. Our study focuses on galaxies in the redshift range $4 < z < 8$. Although other catalogs are available (e.g., Duncan et al. 2019; Whitney et al. 2021; Kodra et al. 2023), we adopt Stefanon et al.’s catalog for convenience because it provides both photometric redshifts and stellar masses. Moreover, the catalog includes self-consistent photometry across 22 bands, covering wavelengths from 0.4 to $8\ \mu\text{m}$, which will benefit our analysis of rest-frame color (Section 4.2).

For sources exposed in more than one telescope pointing, which often appear on the edge of the mosaics, we exclude redundant cutouts and ensure that the surviving cutout has as many available pixels as possible for background estimation and model fitting. After removing galaxies that do not have complete imaging, the final sample contains 669 galaxies (Figure 1; Table A1).

3. IMAGE ANALYSIS

3.1. Model Fitting

We describe the galaxy surface brightness distribution by the Sérsic function,

$$\mu(R) = \mu_e \exp \left\{ -\kappa \left[\left(\frac{R}{R_e} \right)^{1/n} - 1 \right] \right\}, \quad (1)$$

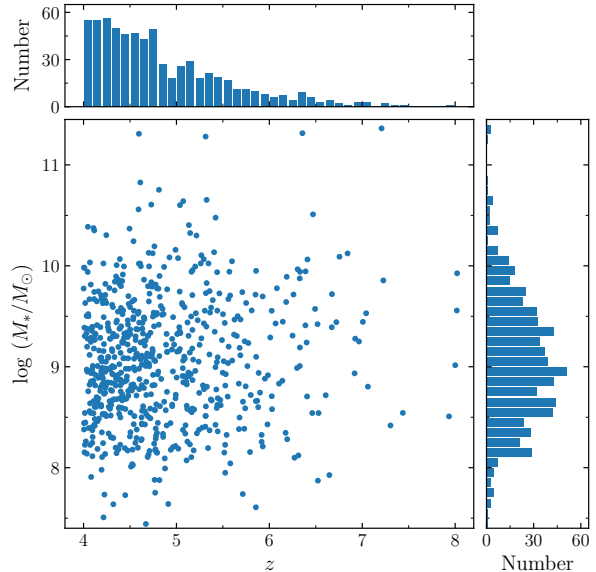


Figure 1. Distribution of redshift and stellar mass of our final sample of 669 galaxies.

where R_e is the effective radius of the galaxy that contains half of the total flux, μ_e is the surface brightness at R_e , Sérsic index n specifies the shape of the profile, and κ is related to n by the incomplete gamma function, $\Gamma(2n) = 2\gamma(2n, \kappa)$ (Ciotti 1991). The light distribution of the galaxy is modeled using `GalfitM` (Häußler et al. 2013; Vika et al. 2013, 2015), a modified version of `Galfit` (Peng et al. 2002; Peng et al. 2010) that can fit simultaneously images in multiple bands. Model parameters across different filters are constrained with a Chebyshev polynomial function whose order the user can control. Previous studies show that constraining n and R_e using a second-order polynomial improves the accuracy and stability of the multi-wavelength model, especially in situations where some bands may suffer from marginal signal-to-noise ratio (Vika et al. 2013).

For subsequent analysis, we generate image cutouts of size 7 times the Kron (1980) radius, a size that contains sufficient pixels for background estimation while still computationally manageable. We use `source_catalog` to measure basic non-parametric quantities, such as the Kron flux, axis ratio (q), and position angle (Θ), which serve as initial guesses for the parametric fits. Following Sun et al. (2024a), contaminating sources in the cutout are masked by dilating the segmentation map with a “growth radius” (Ho et al. 2011; Li et al. 2011). We do not mask contaminating sources that are adjacent to the target galaxy, as they may significantly impact the light distribution of the main galaxy; instead, we simultaneously fit them using multiple components (see Li et al.

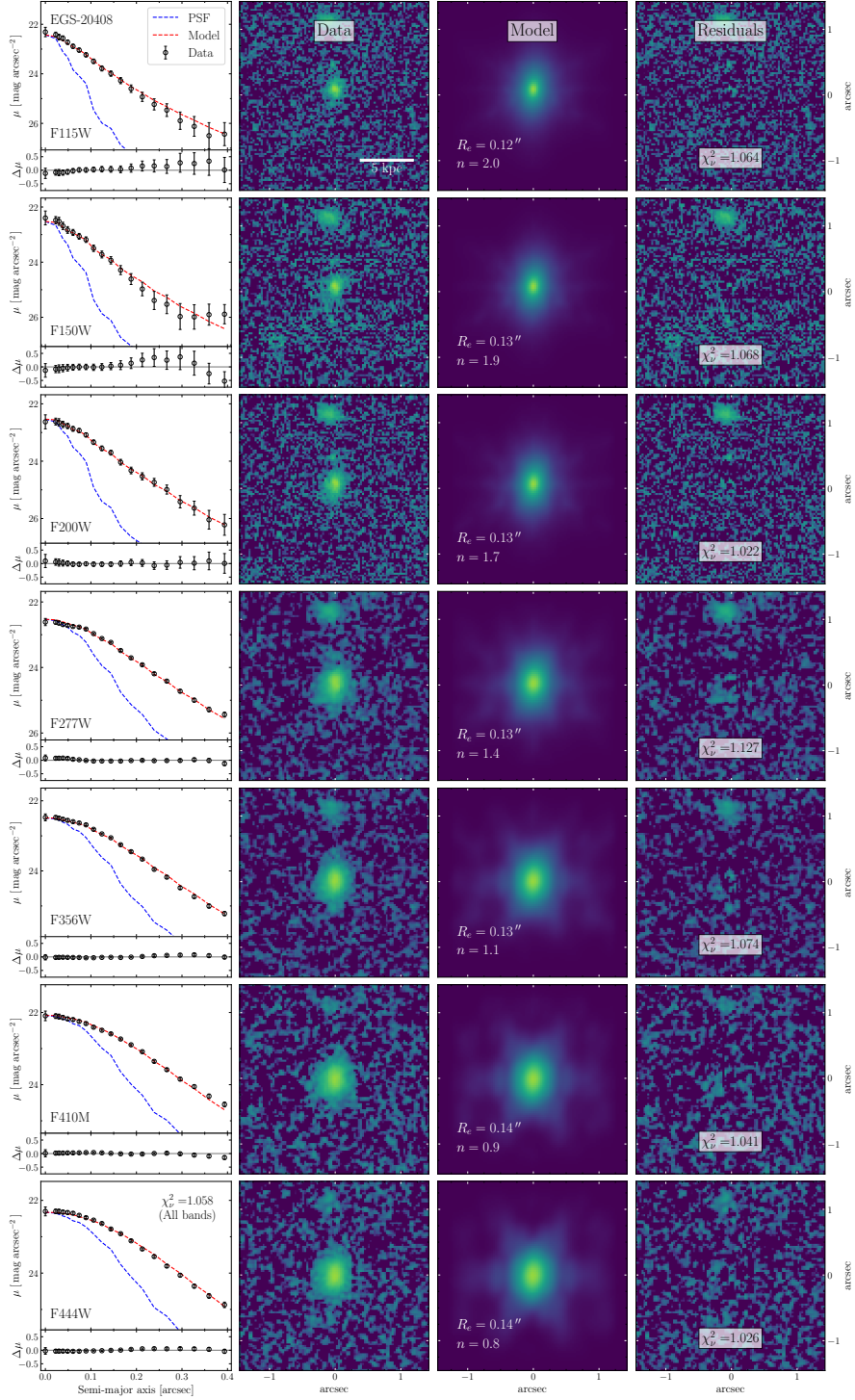


Figure 2. Simultaneous, multiband fitting of the galaxy EGS-20408 (Stefanon et al. 2017) at $z = 5.373$. Rows from top to bottom are the results for the F115W, F150W, F200W, F277W, F356W, F410M, and F444W bands. Columns from left to right are the 1D surface brightness profile, input science image, model image (convolved with the PSF), and residual image. The χ^2_ν for each band is given in the residual image, and the structural parameters are shown in the lower-left corner of the model image. In the 1D profile, the black points with error bars are measured by aperture photometry, the red dashed line shows the model profile, and the blue dashed line represents the PSF, scaled to match the model profile.

2023). We estimate and then subtract the mean value of the local background by excluding all detections, including the target itself, in the cutout with dilating masks. To produce the weight (sigma) image, we scale the error map from the ERR extension such that its level equals the background standard deviation of the science image.

Unlike previous applications of `GalfitM` (e.g., Vika et al. 2015; Sun et al. 2024a), in this study we apply additional constraints to ensure that the parameters n and R_e change monotonically with wavelength, in accord with the observed behavior of galaxies, whose wavelength-dependent radial variation in light profile manifests as color gradients, which are induced by systematic changes in the radial distribution of stellar population and dust reddening (e.g., Kelvin et al. 2012). While invoking a higher-order polynomial to link the structural parameters across different filters may yield a mathematically superior fit, the solution may not be physically meaningful. Hence, we only permit n and R_e to vary linearly with wavelength. The convergence of the fit can be quite sensitive to the initial values of the free parameters. We set the initial value of n to 2, close to the median value found by Sun et al. (2024a), and R_e to the median value of the half-light radius measured using `Photutils` (Bradley et al. 2024). Initially set to the Kron aperture flux, the magnitudes are free to vary with wavelength following a Chebyshev polynomials of order 7. The initial guesses for q and Θ are available from the source detection procedure, and during the fit, these parameters are held constant with wavelength.

Blended sources, when not properly masked, can lead to spurious results (Ono et al. 2024). To guard against this effect, we visually inspect every cutout and its associated segmentation map to assign a flag on its degree of blendness: (1) isolated, (2) blended by adjacent objects that are properly segmented, and (3) heavily blended by a contaminating source. For isolated targets (flag 1), the fitting process is straightforward, and a single Sérsic component suffices to describe the light distribution (Figure 2). Additional components are needed for flag 2 sources, as illustrated in Figure 3, and these more complex fits take longer to converge. The following analysis only makes use of flag 1 and flag 2 sources, and we do not consider the 114 galaxies with flag 3 classification.

3.2. Uncertainties of the Structural Parameters

As with `Galfit`, `GalfitM` estimates the uncertainties using the curvature of the χ^2 surface around the best-fit solution. Many studies have shown that the uncertainties returned by `Galfit` or `GalfitM` are underestimated (Häußler et al. 2022; Nedkova et al. 2024a). To

address this issue, our error estimation is based on mock simulations similar to those described in Zhuang & Ho (2022), where we generate simulated images with known input parameters to resemble real observations. After creating a clean image for each galaxy with its best-fit parameters and convolving it with the PSF model, we mimic realistic observations by adding the Poisson noise of the source and considering background noise levels that differ for every specific image. We generate 100 mocks for each galaxy and fit them with `GalfitM` using the same configuration applied to the actual observations. We adopt the median value of these input-output experiments as the final measurement and incorporate the standard deviation into the final error budget. As discussed in Sun et al. (2024a), the measurements are biased by cosmological effects: the magnitudes of the faintest galaxies at $z = 4$ are underestimated by 0.3 mag, and the sizes are also underestimated, especially for small galaxies. The scatter of the measurements is more significant for galaxies with large Sérsic indices, being most conspicuous at the highest redshifts. We closely follow the mock analysis described in Appendix B of Sun et al. (2024a) to correct the measurement biases and incorporate the uncertainties into the final error budget.

3.3. Quantification of Color Gradient

A variety of strategies have been employed to study the color gradients of high-redshift galaxies (e.g., Miller et al. 2023; Ji et al. 2024; van der Wel et al. 2024). We focus on three simple measures that can be derived straightforwardly from our analysis. Following Vulcani et al. (2014), we define the wavelength variation of the Sérsic index as

$$\mathcal{N} = \frac{n^b}{n^r}, \quad (2)$$

where n^b and n^r denote the Sérsic index measured in the blue and red band, respectively. For example, an early-type galaxy with a redder, more bulge-dominated central region would have a larger value of n at longer wavelengths, resulting in $\mathcal{N} < 1$. In the same spirit, the wavelength variation of the effective radius can be expressed as

$$\mathcal{R} = \frac{R_e^b}{R_e^r}, \quad (3)$$

with R_e^b and R_e^r the effective radius measured in the blue and red band, respectively. A galaxy with an outskirts bluer than its center would have a larger R_e at shorter wavelengths, leading to $\mathcal{R} > 1$. In short, negative color gradients (color profiles that become redder toward the

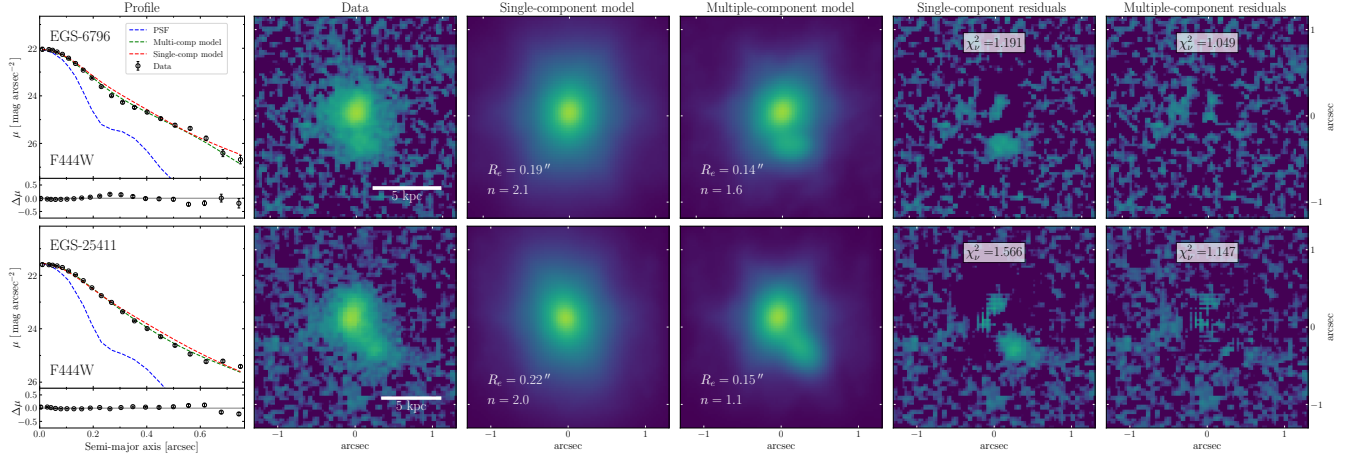


Figure 3. Treatment of blended sources, to avoid biased measurement of structural parameters caused by neighboring source contamination. In the 1D profile, the black points with error bars are measured by aperture photometry, the red dashed line shows the single-component model profile, the green dashed line the multi-component model, which includes the target galaxy and the contaminating neighbor, and the blue dashed line represents the PSF, scaled to match the model profile. It is clear that the outer region of the target galaxy is heavily contaminated by the neighbor, and the additional component is necessary to measure the structural parameters of the target galaxy accurately. The images show, from left to right, the original image, the single-component model, the multi-component model, and the respective residuals for the two models.

center) are characterized by $\mathcal{N} < 1$ and $\mathcal{R} > 1$, whereas positive color gradients (color profiles that become bluer toward the center) are indicated by $\mathcal{N} > 1$ and $\mathcal{R} < 1$. Additionally, we adopt (Marian et al. 2018)

$$\nabla_{b-r} = \frac{\Delta(\mu^b(R) - \mu^r(R))}{\Delta \log R}, \quad (4)$$

where $\mu^b(R)$ and $\mu^r(R)$ are the respective surface brightness profiles as a function of radius R . For the CEERS data in hand, we find that the radial range $R = (0.1 - 1.2) R_e$ effectively captures the color gradient over an area with reliable signal-to-noise ratios. The quantity $\nabla_{F150W-F444W}$ directly measures the color gradient, while \mathcal{R} and \mathcal{N} are indirect proxies for the color gradient that enjoy the privilege of being more robust and less sensitive to artificial effects introduced by the definition of color gradient.

Table A1 summarizes the three measures of color gradient for the sample. We adopt F444W as the red band to maximize the wavelength baseline. For the shortest wavelength band, we choose F150W instead of the bluer F115W band, whose images are often noisy and dominated by clumpy substructure arising from severely dust-attenuated, star-forming clumps. Mostly detected at $> 5\sigma$ significance in HST/WFC3 F160W (Stefanon et al. 2017), our sample essentially is guaranteed to yield robust structural measurements in the NIRCcam F150W band.

To estimate the true uncertainties of the color gradient measurements and to ascertain the limits to which such measurements can be made, we conduct realistic mock

simulations similar to those described in Section 3.2. The mocks are designed to study the influence of galaxy magnitude and structural parameters, the most critical of which is galaxy size, considering that the analysis hinges on the degree to which we can measure the multi-band internal structure of the systems. The input-output experiments, described in Appendix B, show that \mathcal{R} becomes highly uncertain and biased for galaxies with $R_e \lesssim 0''.04$. The measurements for \mathcal{N} and ∇ are even more demanding, starting to break down when $R_e \lesssim 0''.06$. We therefore apply a size cut of $R_e = 0''.06$ to all the bands, a reasonable criterion in view of the PSF sizes of the NIRCcam bands (FWHM $\approx 0''.06 - 0''.16$ (Rigby et al. 2023; Zhuang & Shen 2024). After some experimentation, we find that a magnitude limit of 28 also needs to be imposed. In total, 428 galaxies with no or only moderately serious levels of blending (blending flag 1 or 2; see Section 3.1) satisfy our size and magnitude cut.

4. RESULTS

4.1. Overall Statistics of Color Gradients at $z > 4$

Galaxies generally exhibit color gradients. At low redshifts, most of the gradients are negative, in the sense that the color tends to be redder toward the center (e.g., Zaritsky et al. 1994; Vulcani et al. 2014). Positive color gradients are rare. Merely 10% of galaxies at $z \lesssim 1$ possess positive color gradients (e.g., Pérez-Montero et al. 2016; Carton et al. 2018), and even at $1 < z < 3$ the incidence rises only to $\sim 20\%$ (Simons et al. 2021; Tissera et al. 2022; Sun et al. 2024b). At

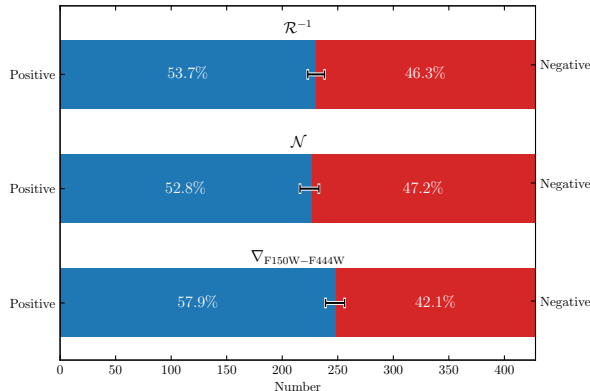


Figure 4. Statistics of color gradients for the 428 galaxies in our sample, given separate for the three methods (\mathcal{R} , \mathcal{N} , $\nabla_{F150W-F444W}$) used to measure color gradient.

the higher redshifts ($z > 4$) probed by our study, most galaxies also have well-established color gradients, but there is a distinctively different balance: a significantly larger proportion of galaxies have positive instead of negative color gradients. Among our final sample of 428 galaxies that are amenable to analysis, the majority ($\sim 50\% - 60\%$) have positive color gradients. Negative color gradients are much less common at high redshifts. Although there are minor differences in the statistics depending on the method used to measure color gradient (\mathcal{R} , \mathcal{N} , or $\nabla_{F150W-F444W}$), the overall trend is robust (Figure 4).

Figure 5 illustrates the two situations encountered in our sample. The left panel shows a typical example of a galaxy with a negative color gradient, EGS-9915 at $z = 4.06$, whose color becomes bluer with increasing radius ($\nabla_{F150W-F444W} = -0.9^{+1.0}_{-1.2}$ mag dex $^{-1}$). For this galaxy, the blue band refers to its rest-frame UV and the red band pertains to its rest-frame near-infrared. The galaxy has a larger R_e ($0''.40$ vs. $0''.35$) and smaller n (0.8 vs. 1.3) in the UV compared to the near-infrared, indicating that it possesses a compact, redder central region and a blue, presumably star-forming extended component. In contrast, the galaxy EGS-13417 at $z = 6.33$ shown on the right panel behaves in the opposite manner: R_e increases ($0''.12$ vs. $0''.14$) while n decreases (3.5 vs. 1.6) toward longer wavelength, leading to a positive color gradient, $\nabla_{F150W-F444W} = 1.5^{+1.0}_{-1.0}$ mag dex $^{-1}$. The red core of EGS-9915 and the blue center of EGS-13417 are obvious from visual inspection of the RGB image (formed by combining F444W, F277W, and F150W). The color gradient is also discernible from the F150W–F444W color image, which was created by matching the PSF of the two bands using

`create_matching_kernel` in `photutils` with the kernel `SplitCosineBellWindow`.

Figure 6 examines whether the incidence of color gradients and the relative proportion of negative versus positive color gradients vary with redshift within the range ($4 < z < 8$) probed here. Because the measurement error increases toward high redshift, we bin the galaxies based on the median error of the measurement, dividing the sample into redshift bins of $4 \leq z < 4.35$, $4.35 \leq z < 4.85$, and $4.85 \leq z < 8$. The median error of each bin is 2 – 3 times smaller than the scatter, and the sample is divided almost equally (Table 1). Galaxies with both negative and positive gradients are clearly common at high redshifts, but the relative incidence of each type remains unchanged within this redshift interval, no matter which of the color gradient measures is considered (Table 1).

4.2. Dependence on Galaxy Properties

Does the color gradient depend on galaxy properties? We investigate the trends between color gradient and galaxy size, stellar mass, and integrated rest-frame $U - J$ color, which is computed using `eazy-py`³, the Python version of `EAZY` (Brammer et al. 2008) commonly used to infer the rest-frame SED of galaxies (e.g., Skelton et al. 2014; van der Wel et al. 2014b; Nedkova et al. 2024a). We adopt the photometric redshifts from CANDELS, a Galactic extinction of $E(B - V) = 0.006$ mag with $R_V = 3.1$ (Schlafly & Finkbeiner 2011), and update the default `tweak_fspe_QSF_12.v3` templates with the bluer templates of Larson et al. (2023)⁴, which give more accurate estimates of the photometric redshift at $z \gtrsim 4$ (e.g., Harvey et al. 2024; Wang et al. 2024). When combining our new, more accurate NIRCcam photometry with the extant panchromatic photometry of the EGS field (Stefanon et al. 2017), we found it advantageous to artificially boost the uncertainties of our measurements by an additional 10% to account for systematic differences between the two different sets of photometry. Note that the rest-frame J band cannot be covered by the reddest NIRCcam band (F444W) at $z > 4$, as for current purposes we must avail to the lower resolution and less sensitive Spitzer photometry. Figure 7 shows the dependence of the color gradient on galaxy properties. In each subpanel, we calculate the running median to accentuate the trend. Each bin includes at least 60

³ <https://eazy-py.readthedocs.io/en/latest/>.

⁴ <https://ceers.github.io/LarsonSEDTemplates>.

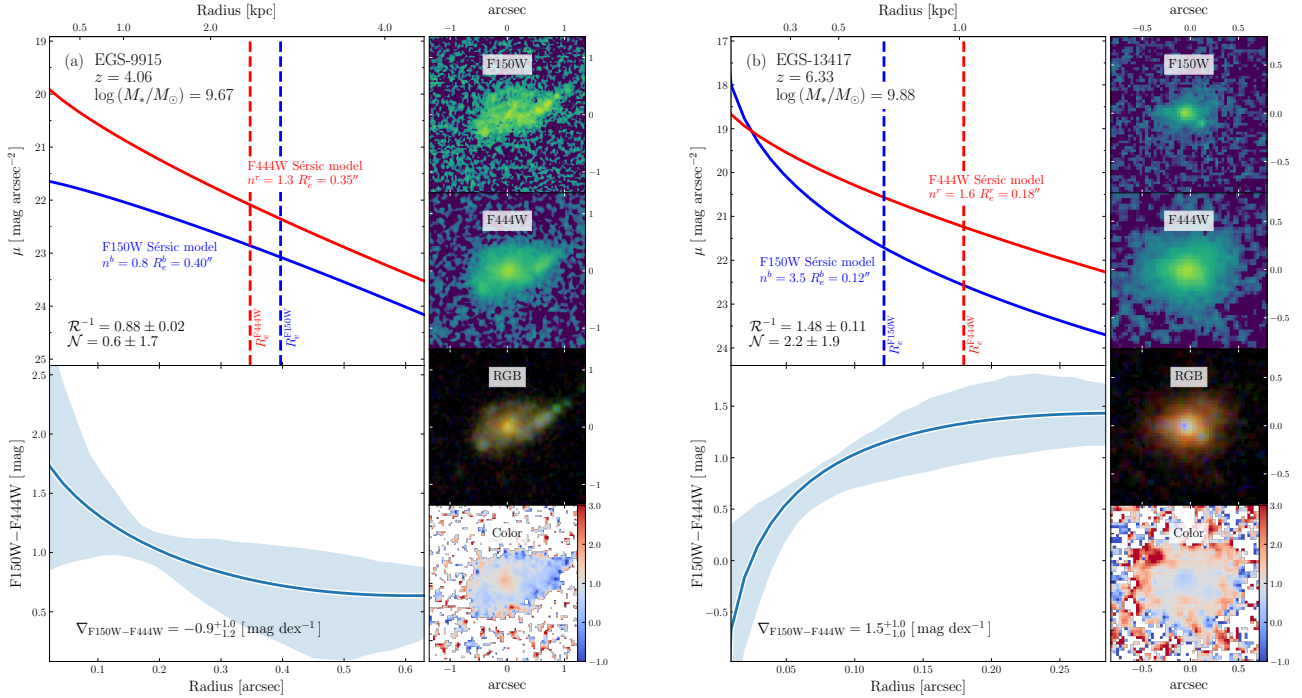


Figure 5. Example of galaxies with (a) negative and (b) positive color gradient in our sample. In each panel, the left column shows the best-fit Sérsic model profile for the F150W and F444W bands (top) and the F150W–F444W color profile (bottom), where the blue shaded area shows the 16th and 84th percentile of the color profile derived by sampling the structural parameter according to its uncertainty. The right column of each panel shows the two-dimensional visualizations of the color gradients: from top to bottom, the panels show the science images from F150W and F444W, the pseudo-color image (red = F444W, green = F277W, blue = F150W), and the PSF-matched F150W–F444W color image.

Table 1. Redshift Evolution of Color Gradient

Redshift Range	Median Redshift	Number	\mathcal{R}^{-1}	$\log \mathcal{N}$	$\nabla_{\text{F150W-F444W}}$
(1)	(2)	(3)	(4)	(5)	(6)
$4 \leq z < 4.35$	4.18	130	$0.96^{+0.19}_{-0.12}$	$0.07^{+0.31}_{-0.20}$	$0.15^{+0.92}_{-0.74}$
$4.35 \leq z < 4.85$	4.59	148	$1.05^{+0.26}_{-0.20}$	$0.07^{+0.45}_{-0.30}$	$0.26^{+1.73}_{-0.78}$
$4.85 \leq z < 8.0$	5.34	150	$1.06^{+0.16}_{-0.25}$	$0.01^{+0.35}_{-0.25}$	$0.22^{+0.94}_{-0.74}$

NOTE— Col. (1): Redshift range. Col. (2): Median redshift. Col. (3): Number of galaxies. Col. (4): Median value of \mathcal{R}^{-1} and the 16th and 84th percent of the distribution. Col. (5): Median value of $\log \mathcal{N}$ and the 16th and 84th percent of the distribution. Col. (6): Median value of $\nabla_{\text{F150W-F444W}}$ and the 16th and 84th percent of the distribution.

galaxies, and the error bars reflect the scatter of the trend, which is estimated from the standard deviation of the data points in each bin.

We find a statistically significant correlation between \mathcal{R}^{-1} and galaxy size, characterized using the effective radius (R_e^{opt}) measured at the optical band closest to rest-frame 5000 Å, such that galaxies with larger size tend to have more negative color gradients (Figure 7,

top row). The trend is robust when considering effective radii measured in other bands (Appendix C). The trend with stellar mass is less steep, but, with p -value = 0.008, formally still qualifies as statistically significant (Table 2). The flattened slope can be explained by the relatively flat relation between the size and stellar mass (Ward et al. 2024) and luminosity (Ono et al. 2024; Sun et al. 2024a) of star-forming galaxies. The trend

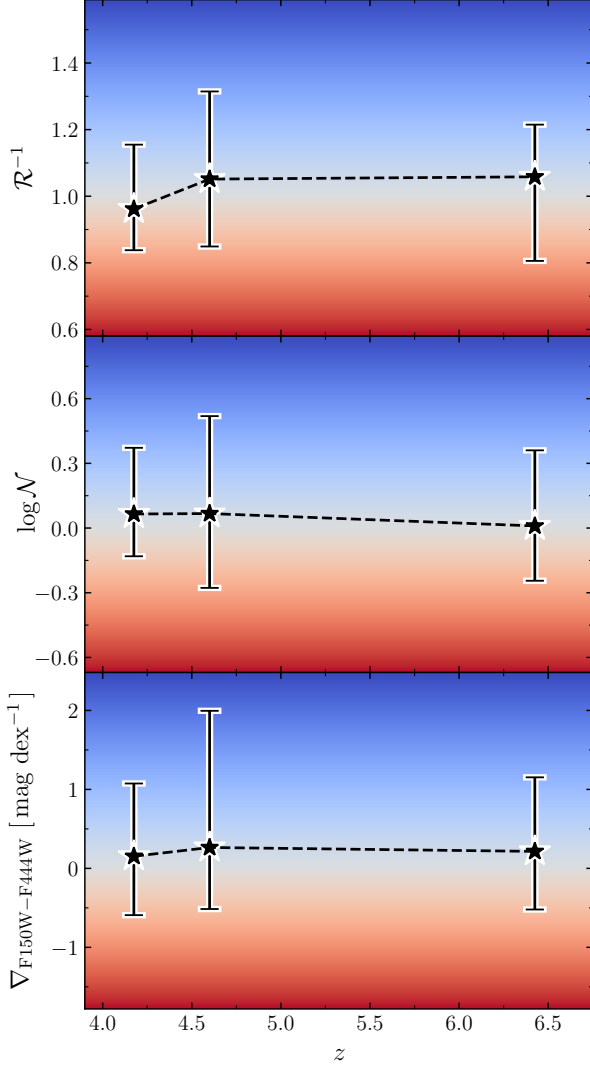


Figure 6. The redshift evolution of the color gradient, quantified using the variation of the effective radius \mathcal{R} (Equation 3; top), variation of the Sérsic index \mathcal{N} (Equation 2; middle), and the color gradient $\nabla_{\text{F150W-F444W}}$ (Equation 4; bottom). The black stars indicate the median value for each redshift bin, with the error bars giving the 16th and 84th percentile of the distribution. The background gradient describes the region where the color gradient is positive (blue) or negative (red).

with stellar mass naturally extends to $U - J$ color, insofar as more massive galaxies are redder. The case for \mathcal{N} is more ambiguous (Figure 7, middle row), which is understandable because the Sérsic indices of faint, high-redshift galaxies are much more difficult to measure than their effective radii (Sun et al. 2024a). Although \mathcal{N} is formally uncorrelated with galaxy size, the dependence on stellar mass is statistically robust (p -value < 0.001), consistent with the tendency for high-mass systems to exhibit negative color gradients and low-mass systems

Table 2. Best-fit Results of Linear Regression

Label	X	s	X_0	p -value
(1)	(2)	(3)	(4)	(5)
$\mathcal{R}^{-1} = s(X - X_0) + 1$				
(a)	$\log(R_e^{\text{opt}}/\text{kpc})$	-0.31 ± 0.07	0.15 ± 0.04	0.000*
(b)	$\log(M_*/M_\odot)$	-0.06 ± 0.02	10.00 ± 3.98	0.008*
(c)	$U - J$ (mag)	-0.12 ± 0.03	1.03 ± 0.30	0.001*
(d)	q	-0.07 ± 0.08	1.36 ± 1.69	0.420
(e)	$\log n^{\text{opt}}$	0.08 ± 0.06	-0.65 ± -0.47	0.163
$\log \mathcal{N} = s(X - X_0)$				
(f)	$\log(R_e^{\text{opt}}/\text{kpc})$	-0.15 ± 0.09	0.61 ± 0.42	0.126
(g)	$\log(M_*/M_\odot)$	-0.11 ± 0.03	9.96 ± 3.84	0.000*
(h)	$U - J$ (mag)	-0.15 ± 0.04	1.17 ± 0.40	0.001*
(i)	q	-0.23 ± 0.11	0.91 ± 0.50	0.035*
(j)	$\log n^{\text{opt}}$	0.13 ± 0.07	-0.62 ± -0.37	0.069
$\nabla_{\text{F150W-F444W}} = s(X - X_0)$				
(k)	$\log(R_e^{\text{opt}}/\text{kpc})$	-1.27 ± 0.29	0.28 ± 0.08	0.000*
(l)	$\log(M_*/M_\odot)$	-0.49 ± 0.09	9.91 ± 2.51	0.000*
(m)	$U - J$ (mag)	-0.76 ± 0.13	1.07 ± 0.22	0.000*
(n)	q	-0.67 ± 0.33	1.12 ± 0.62	0.046*
(o)	$\log n^{\text{opt}}$	0.11 ± 0.22	-3.71 ± -7.74	0.632

NOTE— Col. (1): The label of the linear regression. Col. (2): The galaxy property that serves as the independent variable X in the regression. Col. (3): The best-fit slope of the linear regression. Col. (4): The typical value X_0 of the independent variable X that makes the estimated variation (i.e., the estimated value of \mathcal{R} or \mathcal{N} at X_0) equals 1. For $\nabla_{\text{F150W-F444W}}$, X_0 refers to the typical value that makes $\nabla_{\text{F150W-F444W}} = 0$. Col. (5): The probability of accepting the null hypothesis that the slope is zero (i.e., no statistical correlation). *We take p -value < 0.05 as the probability of rejecting the null hypothesis of no correlation.

to reverse the trend. Again, the trend with stellar mass extends to $U - J$ color. Among the three estimators of the color gradient, the most pronounced trends emerge with $\nabla_{\text{F150W-F444W}}$ (Figure 7, bottom row).

Additional insight can be gleaned from considering the distribution of color gradients on the stellar mass-size and stellar mass-color diagrams, which are shown on the top and bottom rows of Figure 8, respectively. Here, it can be seen that at *fixed* stellar mass the color gradient depends on galaxy size: as the effective radius increases, the color gradient systematically shifts from positive to negative. These trends are most clearly seen when the color gradient is estimated using \mathcal{R} or $\nabla_{\text{F150W-F444W}}$, but it is also apparent when \mathcal{N} is used. Similarly, at a given stellar mass the color gradients vary systematically with $U - J$ color: bluer galaxies have blue centers and redder exteriors.

Lastly, we examine whether any connection can be found between color gradient and galaxy morphology. Using the Sérsic index in the rest-frame optical (n^{opt}) as a crude guide to morphology, we find no statistically meaningful relation between n^{opt} and any of the

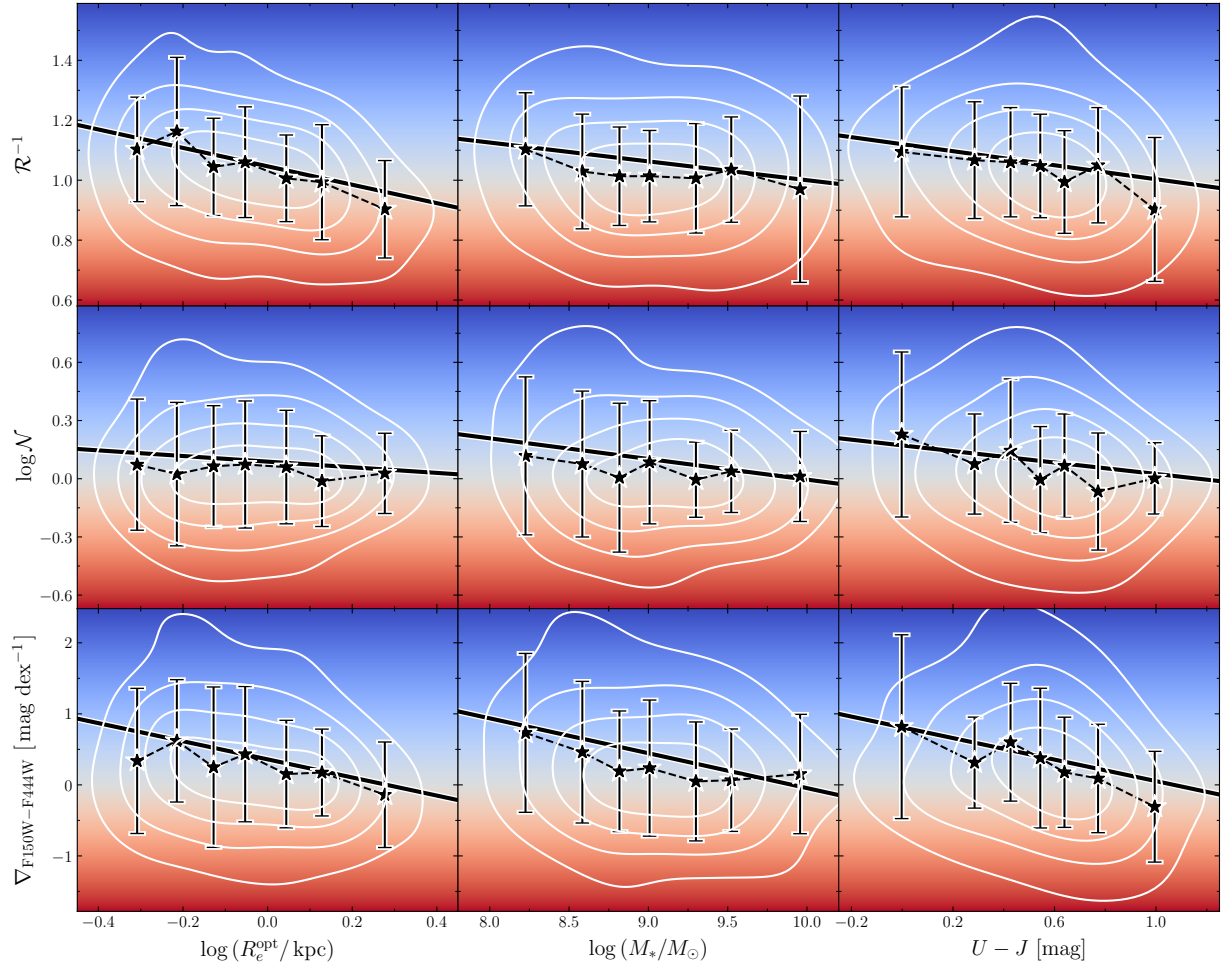


Figure 7. Dependence on galaxy properties of the color gradient, quantified using (top) the variation of the effective radius \mathcal{R} (Equation 3), (middle) variation of the Sérsic index \mathcal{N} (Equation 2), and (bottom) the color gradient $\nabla_{F150W-F444W}$ (Equation 4). From left to right, the columns show the dependence on galaxy optical effective radius (R_e^{opt}), stellar masses (M_*), and rest-frame $U - J$ color. The white contours denote the density distribution of the data points, the stars show the running median of the data binned so that each bin contains at least 60 galaxies, and the error bars indicate the standard deviation. The solid line gives the best-fit linear regression. The background gradient denotes the region where the color gradient is positive (blue) or negative (red).

three measures of color gradient (Table 2). We do see a very tentative link between color gradient and galaxy axial ratio (q). The mild correlation between q and \mathcal{N} or $\nabla_{F150W-F444W}$ hints at the possibility that positive color gradients are more likely to be found in disk-like or prolate systems (Tomassetti et al. 2016).

In summary, both positive and negative color gradients exist in $z > 4$ galaxies, but the relative proportion of positive gradients becomes much more prevalent than at low redshifts. Notably, the sign of the color gradient depends systematically on galaxy properties. Whereas galaxies with negative color gradients are generally larger, more massive, and redder, positive color gradients preferentially occur in smaller, low-mass, bluer, possibly more disk-dominated or prolate systems.

For any given stellar mass, more compact galaxies are more likely to have a positive color gradient.

5. DISCUSSION

5.1. Origin of the Color Gradients

Color gradients in galaxies principally arise from radial variations in stellar population, dust reddening, or both. To evaluate which factor is most relevant, Figure 9 shows the UVJ diagram (Williams et al. 2009), a widely used tool to gauge the star formation activity and dust attenuation of galaxies according to their rest-frame colors (Wang et al. 2017; Miller et al. 2022, 2023). The lower left corner of the diagram is usually occupied by star-forming galaxies with little dust attenuation, because of their young stellar population and steep UV continuum slope. We separate the galax-

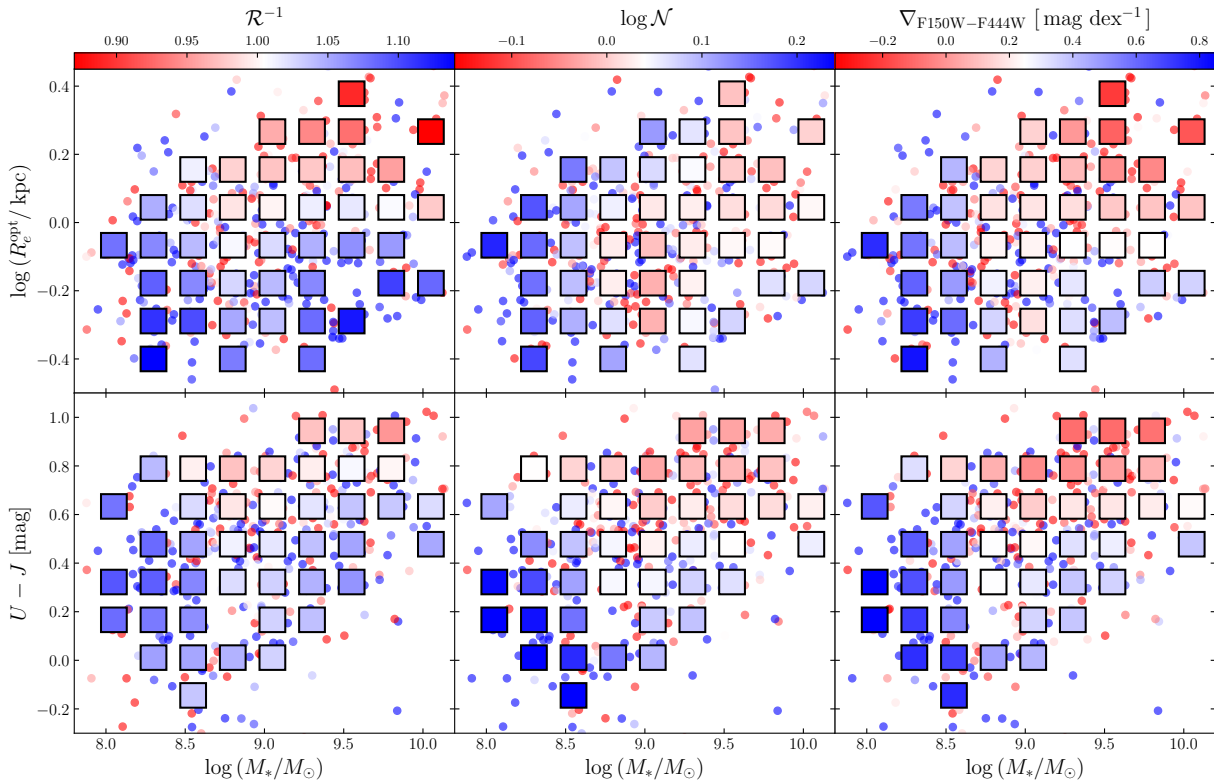


Figure 8. The stellar mass-size and stellar mass-color plane of our sample. From left to right, the columns quantify the color gradient using \mathcal{R}^{-1} , $\log \mathcal{N}$, and $\nabla_{F150W-F444W}$, whose strength is indicated by the color bar on the top. The squares denote median values of at least five objects within a box of size 0.25 dex in $\log M_*$ and 0.11 dex in $\log R_e^{\text{opt}}$ or 0.15 mag in $U - J$, after performing a locally weighted regression smoothing using the Python package LOESS (Cappellari et al. 2013).

ies into three categories based on their color gradient: $\nabla_{F150W-F444W} < -0.5 \text{ mag dex}^{-1}$ are considered to have a robust negative color gradient, $\nabla_{F150W-F444W} > 0.5 \text{ mag dex}^{-1}$ denote a definitive positive color gradient, and those with $-0.5 \text{ mag dex}^{-1} \leq \nabla_{F150W-F444W} \leq 0.5 \text{ mag dex}^{-1}$ as having an inconclusive or flat color gradient. Our sample in the UVJ diagram populates the regime of dust-free, star-forming galaxies. The slight, but systematic offset between objects of opposing color gradients follows from the propensity of galaxies with positive color gradients to have overall bluer colors (Section 4.2). The same applies to sources with negative color gradients, which are ostensibly redder because of their larger stellar masses (Figure 7, bottom row). Applying `eazy-py` to model the full rest-frame UV-to-NIR SED using all available broadband photometry, we find that galaxies with positive color gradients are best fit with a distinctly younger spectral template, as evidenced by their more prominent UV emission and shallower 4000 Å break (Figure 10a). Intriguingly, the stellar population difference between the two populations is confined exclusively to massive galaxies ($M_* \geq 10^9 M_\odot$; Figure 10b) and is hardly perceptible among less massive systems ($M_* < 10^9 M_\odot$; Figure 10c).

Cosmological simulations of massive ($M_* \approx 10^9 - 10^{10} M_\odot$) galaxies at $z \approx 2$ produce “blue nuggets” with central star formation enhanced by violent disk instability, minor mergers, and counter-rotating streams (Zolotov et al. 2015). This “compaction” phase of galaxy evolution has garnered support from recent JWST/MIRI observations that spatially map dust-obscured star formation in $z \lesssim 2.5$ galaxies (Magnelli et al. 2023; Lyu et al. 2024). Examples of “outside-in” growth also can be found much closer to home. For instance, Tuttle & Tonnesen (2020) identified a group of 118 $z < 0.05$ “BreakBRDs” (break bulges in red disks) galaxies that feature truncated disk star formation and a blue star-forming core, whose central concentration of gas and subsequent star formation may be traced plausibly to the low angular momentum of their circumgalactic medium (Tonnesen et al. 2023; Stark et al. 2024). Analyzing the half-light radii measured from HST F275W and F160W images of $0.05 < z < 0.3$ galaxies selected from the GOODS-North field, Cheng et al. (2020) concluded that while high-mass galaxies conform with the expectations of the conventional inside-out growth mode, some galaxies with $M_* < 10^8 M_\odot$ display small-

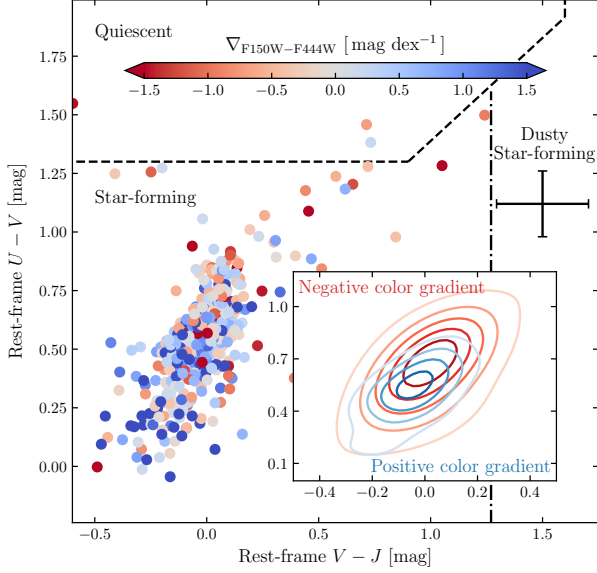


Figure 9. UVJ diagram for the galaxies in our sample, color-coded by $\nabla_{F150W-F444W}$ (Equation 4), whose strength is indicated by the color bar. The dashed lines are the criteria for separating star-forming and quiescent galaxies (Williams et al. 2009), while the dot-dashed line defines the dusty star-forming galaxies (Miller et al. 2023). The inset subpanel shows the kernel density estimation of the population with negative color gradient (red contours) and positive color gradient (blue contours). The error bar indicates the median value of uncertainties of the rest-frame colors, as inferred using `eazy-py` (Section 4.2).

scale UV structures consistent with ongoing central star formation.

The high incidence of positive color gradients revealed in our study is qualitatively consistent with the prevalence of compact UV morphology reported in $z \gtrsim 5$ galaxies (e.g., Harikane et al. 2024; Morishita et al. 2024). The compactness of these UV-bright systems suggests that star formation proceeds through a violent central starburst, possibly triggered by angular momentum dissipation due to mergers or in situ instabilities (Dekel et al. 2020). Moreover, we find that positive color gradients preferentially inhabit among low-mass ($M_* \lesssim 10^9 M_\odot$) galaxies. A similar trend is reported for the $4 \leq z \leq 10$ galaxies studied by Tripodi et al. (2024), whose emission-line equivalent widths are most intense in the centers of low-mass systems. Their stacking analysis also tentatively suggests that the metallicity gradient in these galaxies is inverted. Low-mass galaxies may be particularly prone to centrally concentrated star formation because their gas depletion time is shorter than the replenishment time, and common merger-driven spin flips (Tacchella et al. 2016; Dekel et al. 2020) facilitate inward mass transport. Moreover, the apparent connec-

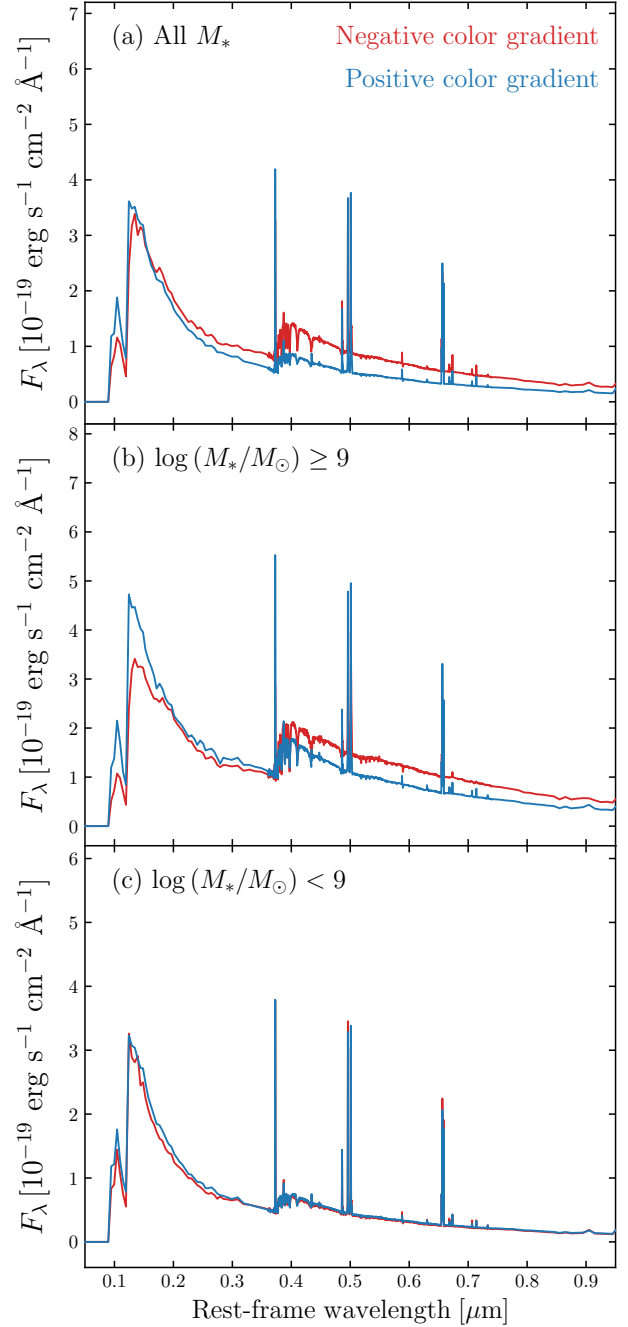


Figure 10. The rest-frame SEDs of galaxies with (a) all stellar masses, (b) $\log(M_*/M_\odot) \geq 9$, and (c) $\log(M_*/M_\odot) < 9$ having negative color gradient (red) and positive color gradient (blue). The solid lines show the median value of the best-fit template spectra, with the shaded area denoting the 16th and 84th percentile of the distribution.

tion between positive color gradients and smaller axis ratios, although statistically only marginal (Table 2), might arise naturally if low-mass galaxies are initially prolate, a notion advanced by cosmological simulations (Lapiner et al. 2023) and supported by observations (van

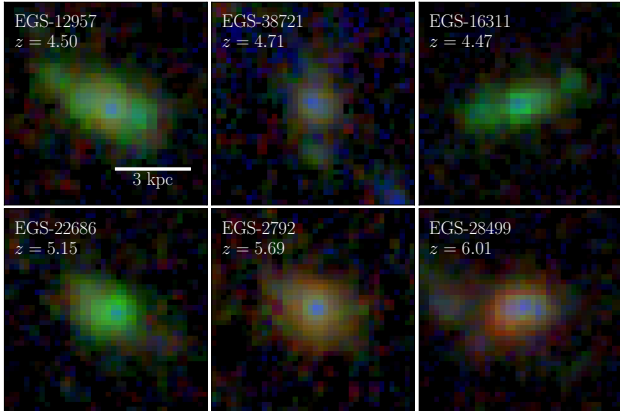


Figure 11. Pseudo-color images of galaxies with positive color gradients that show evidence of hosting a central point-like source (where red = F444W, green = F277W, and blue = F150W).

der Wel et al. 2014a; Zhang et al. 2019; Pandya et al. 2024).

5.2. The Role of Active Galactic Nuclei

Active galactic nuclei (AGNs) complicate the interpretation of our results. To the extent that a nuclear point source, if unobscured, boosts the optical-UV flux of the central region and artificially alters the structural parameters of the morphological analysis, an AGN can be confused with compact star formation. This is especially worrisome in light of the unexpectedly high abundance of high-redshift AGNs discovered in the JWST era (e.g. Kokorev et al. 2024; Labbé et al. 2024). Careful inspection of the results of our two-dimensional image analysis reveals that 28 galaxies (6.5% of 428 galaxies) are better fit by adding an additional point-source component to the underlying Sérsic model for the galaxy. These are flagged as potential AGN host galaxies⁵ in Table A1, and we conservatively remove them from our statistical analysis, although our main conclusions are not affected by this choice. Most of them (22/28; 78%) exhibit a positive color gradient, the rest negative. Figure 11 showcases some galaxies whose central colors are clearly influenced by a prominent blue core, which is likely to be an active nucleus. One of the examples, EGS-28499, refers to the spectroscopically identified broad-line AGN CEERS 00397 (Harikane et al. 2023). The presence of an AGN core can distort substantially the inferred color gradient of the underlying host galaxy. An example is given in Figure 12, which shows that in the case of EGS-

12957 removing the nuclear point source drastically affects the Sérsic index of the galaxy, especially in the F150W band, such that its color gradient proxy switches from an original value of $\mathcal{N} = 3.1$ to a nucleus-removed value of $\mathcal{N} = 0.6$, flipping the color gradient from positive to negative.

5.3. Comparison with Previous Studies

Galaxies at low redshifts are generally significantly larger in the rest-frame UV than in the optical because of the preponderance of negative color gradients (e.g., van der Wel et al. 2014b; Shibuya et al. 2015). In their investigation of galaxies across the main sequence at $z \approx 0.7 - 1.5$, Nelson et al. (2016) argued that the increasing size discrepancy between the H α and stellar continuum morphology constitutes evidence of inside-out growth. This trend becomes less pronounced at $z \approx 1 - 3$ (Suess et al. 2019), and by $z \gtrsim 4$ we find that an increasingly large fraction of galaxies sport positive instead of negative color gradients. Similar results were obtained by Morishita et al. (2024) in their study of the UV and optical sizes of 149 $z \geq 4$ galaxies, by Jia et al. (2024) with the comparison of rest-frame $0.45 \mu\text{m}$ and $1.0 \mu\text{m}$ sizes for $z \gtrsim 4$ galaxies in JADES, as well as by Treu et al. (2023) for their sample of 19 Lyman-break galaxies at $z > 7$. Interestingly, the sign and magnitude of the gradient depends on galaxy mass (and thus, indirectly, on galaxy size), such that more massive galaxies exhibit steeper negative color gradients than low-mass systems. Suess et al. (2019) conclude that the strength of the negative color gradient is stronger for galaxies of larger size, higher stellar mass, and redder color, precisely the trends found here for galaxies at $z > 4$. In contrast to the inside-out growth for massive systems, galaxies of intermediate stellar mass ($M_{\star} \approx 10^9 M_{\odot}$) tend to have relatively flat color profiles, an effect attributed to coherent star formation across all radii in this mass regime (van Dokkum et al. 2013; Tacchella et al. 2018; Nelson et al. 2021; Hasheminia et al. 2024). And by the time we reach even lower masses ($M_{\star} \lesssim 10^9 M_{\odot}$), positive color gradients outnumber negative ones.

6. SUMMARY

We conduct a comprehensive study of the color gradients of 669 high-redshift ($4 < z < 8$) galaxies using the NIRCcam images from the JWST CEERS program. The structural parameters of the galaxies are obtained by simultaneously fitting the seven-band images using the two-dimensional analysis code `GalfitM`. We quantify the color gradient using three empirical proxies (\mathcal{R} , \mathcal{N} , $\nabla_{\text{F150W-F444W}}$) that can be derived robustly from the parametric fits, whose uncertainties can be inferred from the extensive mock simulations performed

⁵ The true physical nature of the central point source remains ambiguous, however, in the absence of reliable spectroscopic information.

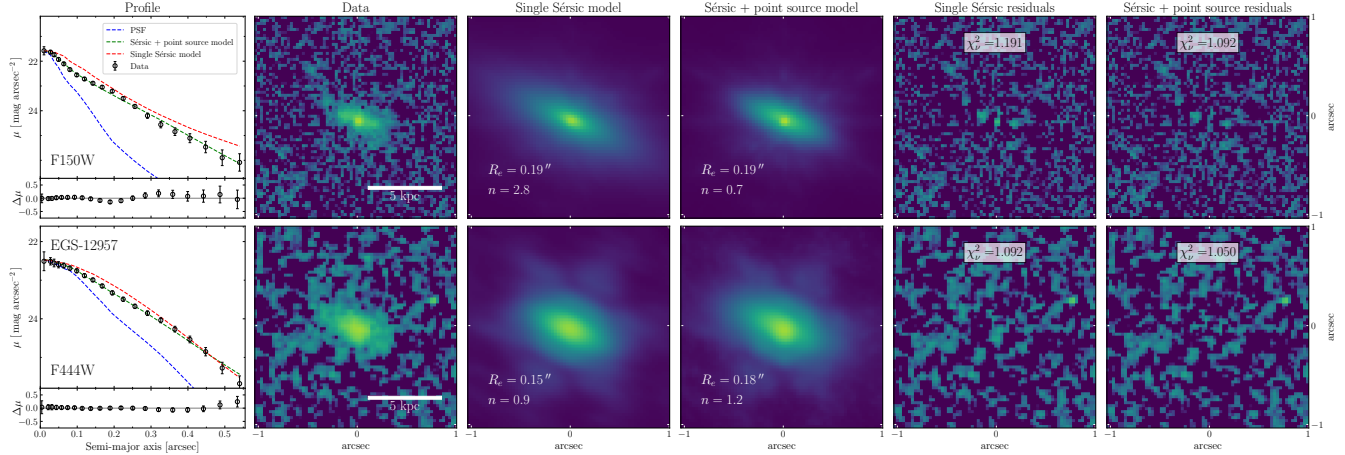


Figure 12. Influence of a “blue nucleus” on the measurements, for F150W (top) and F444W (bottom). In the 1D profile, the black points with error bars are measured by aperture photometry, the red dashed line shows the single-Sérsic model, the green dashed line refers to the Sérsic+point source model, and the blue dashed line represents the PSF, scaled to match the model profile. The lower panel of the left column shows the residuals between the Sérsic+point source model and the data. The images show, from left to right, the original image, the single-Sérsic model, the Sérsic+point source model, and the respective residuals for the two models. It is clear that including the nucleus component improves the quality of the fit, and that the additional component is necessary to measure accurately the structural parameters of the host galaxy.

by Sun et al. (2024a). The main results are summarized as follows:

1. Both positive and negative color gradients are present in $z > 4$ galaxies, with the frequency of positive gradients ($\sim 50\% - 60\%$) markedly higher than found at lower redshifts ($\sim 10\% - 20\%$). Within the limitations of the current sample size, we discern no evidence of redshift evolution in color gradient within the range $4 < z < 8$.
2. The color gradients principally reflect radial variations in stellar population instead of dust reddening. While emission from a point-like active nucleus can present a significant source of contamination and confusion in the interpretation of the color gradients, we argue that our main conclusions are robust against AGN contamination.
3. The sign and magnitude of the color gradient depend systematically on the global properties of the galaxy, such that galaxies of higher stellar mass, larger size, and redder integrated color possess increasingly steeper negative color gradients indicative of inside-out growth. Galaxies of lower stellar mass, here defined by $M_\star \lesssim 10^9 M_\odot$, more compact size, and bluer colors have preferentially positive color gradients, consistent with centrally concentrated star formation.

Future work can be improved by enlarging the sample using other JWST deep surveys, such as COSMOS-Web (Casey et al. 2023), JADES (Eisenstein et al. 2024), and

NGDEEP (Bagley et al. 2024). We can gain deeper insights into the origin of the color gradients by jointly considering additional physical properties of the galaxies, including their star formation rate, dust attenuation, and AGN activity, which can be estimated by fitting their broadband spectral energy distribution. Finally, although we have ruled out the possibility that nuclear activity is the main culprit of the excess positive color gradients in our sample, we are still unsure to what extent AGNs influence the internal properties of galaxies at high redshifts. Adding spectral information, which will become available for increasingly large JWST samples, will be highly informative.

- 1 This research was supported by the National Key R&D
- 2 Program of China (2022YFF0503401), the National Science
- 3 Foundation of China (11991052, 12233001), and
- 4 the China Manned Space Project (CMS-CSST-2021-
- 5 A04, CMS-CSST-2021-A06). We thank Chang-Hao
- 6 Chen, Fangzhou Jiang, Limin Lai, Ruancun Li, Yang
- 7 Li, Zhaoyu Li, Chao Ma, Jinyi Shanguan, and Ming-
- 8 Yang Zhuang for discussions and technical advice.

Facilities: JWST (NIRCam)

Software: Astropy (The Astropy Collaboration et al. 2013), Galfit (Peng et al. 2002; Peng et al. 2010), GalfitM (Häußler et al. 2013; Vika et al. 2013), eazy-py (Brammer et al. 2008), Photutils (Bradley et al. 2024),

Matplotlib (Hunter 2007), NumPy (Harris et al. 2020),
SciPy (Virtanen et al. 2020)

APPENDIX

A. COLOR GRADIENT ANALYSIS

Table A1 presents the catalog of parameters derived from the color gradient analysis.

Table A1. Multi-wavelength Structural Parameter Catalog Entries

Column	Format	Name	Description
1	STRING	Name	Object name from Stefanon et al. (2017)
2	DOUBLE	RAdeg	Right ascension in decimal degrees (J2000.0)
3	DOUBLE	Decdeg	Declination in decimal degrees (J2000.0)
4	DOUBLE	z	Redshift
5	DOUBLE	logMs	Stellar mass from Stefanon et al. (2017)
6	DOUBLE	e_logMs	Mean error on $\log M_*$
7	DOUBLE	F150WRe	Half-light radius R_e in F150W
8	DOUBLE	e.F150WRe	Mean error on R_e in F150W
9	DOUBLE	F150Wn	Sérsic index n in F150W
10	DOUBLE	e.F150WRe	Mean error on n in F150W
11	DOUBLE	F444WRe	Half-light radius R_e in F444W
12	DOUBLE	e.F444WRe	Mean error on R_e in F444W
13	DOUBLE	F444Wn	Sérsic index n in F444W
14	DOUBLE	e.F444Wn	Mean error on n in F444W
15	DOUBLE	q	Axis ratio q
16	DOUBLE	e_ q	Mean error on q
17	DOUBLE	PA	Position angle Θ
18	DOUBLE	e_PA	Mean error on Θ
19	STRING	RestFrameOpticalBand	Rest-frame optical band
20	DOUBLE	ReOpt	Half-light radius R_e in the rest-frame optical band
21	DOUBLE	e_ReOpt	Mean error on ReOpt
22	DOUBLE	nOpt	Sérsic index n in the rest-frame optical band
23	DOUBLE	e_nOpt	Mean error on nOpt
24	DOUBLE	Umag	Apparent magnitude in rest-frame U from <code>eazy-py</code>
25	DOUBLE	e_Umag	Mean error on Umag
26	DOUBLE	Vmag	Apparent magnitude in rest-frame V from <code>eazy-py</code>
27	DOUBLE	e_Vmag	Mean error on Vmag
28	DOUBLE	Jmag	Apparent magnitude in rest-frame J from <code>eazy-py</code>
29	DOUBLE	e_Jmag	Mean error on Jmag
30	DOUBLE	ChisqGalfitM	Reduced chi-square from <code>GalfitM</code>
31	LONG	FlagBLD	Blendness flag
32	DOUBLE	F115Wfnu	Flux in F115W
33	DOUBLE	e_F115Wfnu	Mean error on flux in F115W
34	DOUBLE	F150Wfnu	Flux in F150W
35	DOUBLE	e_F150Wfnu	Mean error on flux in F150W
36	DOUBLE	F200Wfnu	Flux in F200W
37	DOUBLE	e_F200Wfnu	Mean error on flux in F200W

Continued on Next Page...

Table A1 – Continued

Column	Format	Name	Description
38	DOUBLE	F277Wfnu	Flux in F277W
39	DOUBLE	e_F277Wfnu	Mean error on flux in F277W
40	DOUBLE	F356Wfnu	Flux in F356W
41	DOUBLE	e_F356Wfnu	Mean error on flux in F356W
42	DOUBLE	F410Mfnu	Flux in F410M
43	DOUBLE	e_F410Mfnu	Mean error on flux in F410M
44	DOUBLE	F444Wfnu	Flux in F444W
45	DOUBLE	e_F444Wfnu	Mean error on flux in F444W
46	LONG	FlagHOST	Possible AGN host galaxy flag

B. MOCK TESTS OF THE COLOR GRADIENT PROXIES

We present a simple illustration of the mock analysis described in Section 3.2, by illustrating some typical examples. These scenarios span a range of parameter space that covers our sample well. For each of the three color gradient proxies (Equations 2–4), we study the possible bias, defined as the difference between the input and the output parameter values, for three representative input values, as a function of galaxy size (represented by R_e^{F444W}) and source brightness (represented by F150W magnitude). We consider four bins of galaxy size ($R_e^{\text{F444W}} < 0''.032$, $0''.032 - 0''.060$, $0''.060 - 0''.112$, and $0''.112 - 0''.161$), six values of the Sérsic index ($n = 0.71, 1.09, 1.66, 2.53, 3.86, 5.90$), and 10 bins in source brightness spanning $\text{F150W} = 20 - 29$ mag.

For the proxy that describes the wavelength variation of the effective radius, we choose $\mathcal{R} = 0.53, 1.00, \text{ and } 1.87$ as representative of the observed parameter space. Figure B1 shows that $\Delta \log \mathcal{R}$ can be measured up to ~ 0.21 dex for all but the first size bin ($R_e^{\text{F444W}} < 0''.032$) and for $\text{F150W} \gtrsim 28$ mag. As for the proxy that describes the wavelength variation of the Sérsic index, we choose $\mathcal{N} = 0.66, 1.00, \text{ and } 1.53$ as representative of the observed parameter space. Similarly, Figure B2 shows that \mathcal{N} is accurate ($\Delta \log \mathcal{N} \lesssim 0.29$ dex) for all but $R_e^{\text{F444W}} \lesssim 0''.060$ and $\text{F150W} \gtrsim 28$ mag. The overall assessment for \mathcal{N} also applies to $\nabla_{\text{F150W-F444W}}$ (Figure B3). We conclude that reliable measurements can be obtained for all three proxies of the color gradient so long as $R_e^{\text{F444W}} > 0''.06$ and $\text{F150W} < 28$ mag.

C. ROBUSTNESS OF THE DEPENDENCE OF \mathcal{R} ON GALAXY SIZE

Section 4.2 (Figure 7, top row) describes the inverse correlation between \mathcal{R}^{-1} and galaxy size, which was represented by R_e^{opt} , the effective radius measured at the optical band closest to rest-frame 5000 Å. Figure C1 verifies that the inverse correlation remains significant for different choices of effective radius, although the slope becomes shallower toward effective radii measured at longer wavelength.

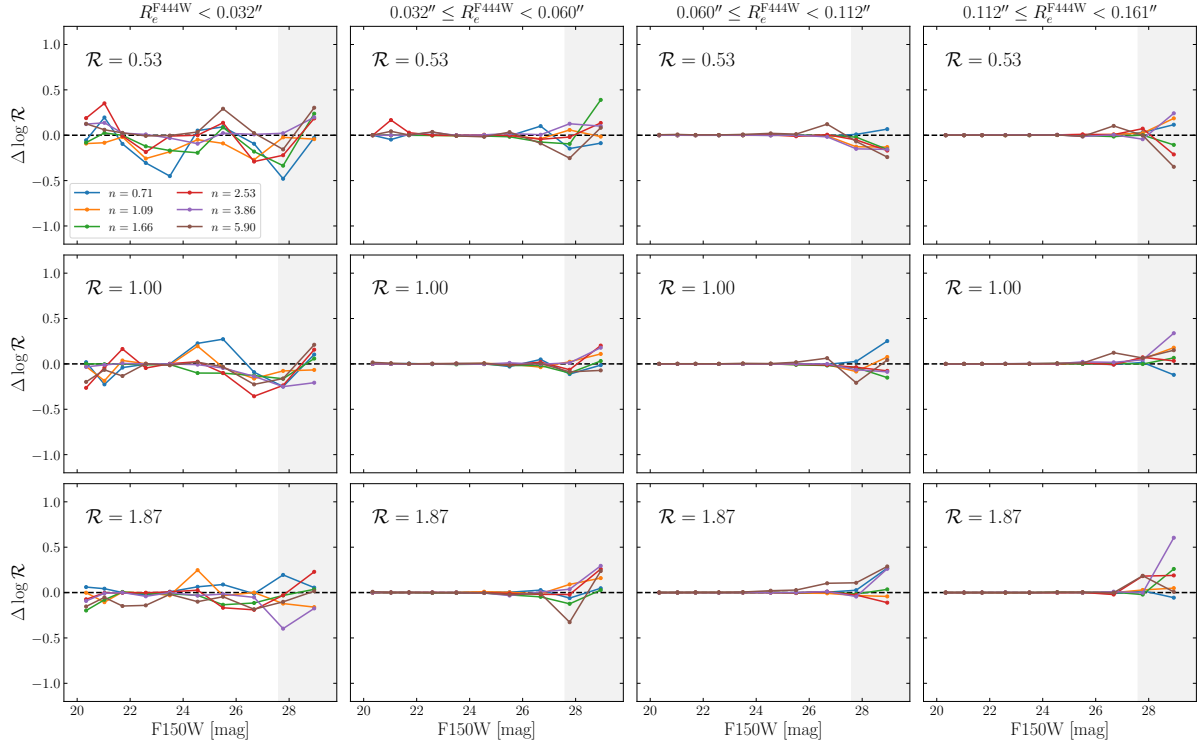


Figure B1. The bias of \mathcal{R} as a function of magnitude in F150W, for $\mathcal{R} = 0.53$ (top), 1.00 (middle), and 1.87 (bottom), and, for columns from left to right, different values in input R_e^{F444W} . The colors indicate the input values of the Sérsic index n at F444W. The grey-shaded region marks the magnitude range below 5σ detection at HST/WFC3 F160W.

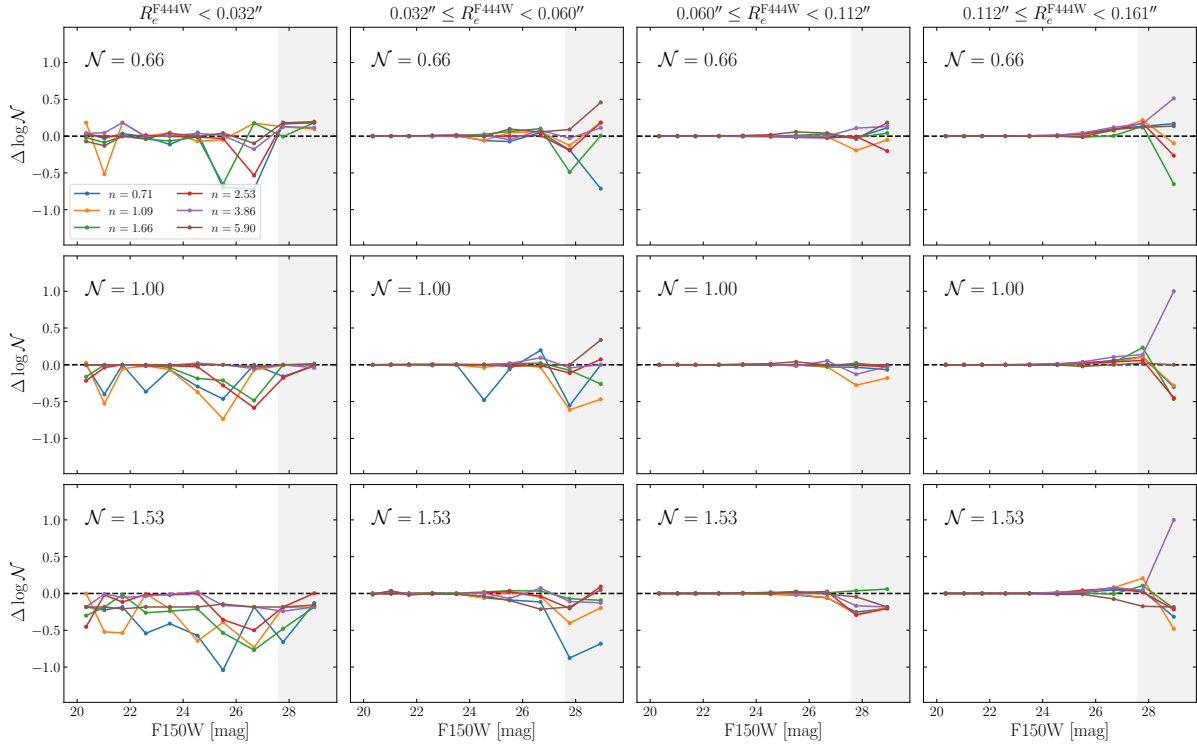


Figure B2. As in Figure B1, but for the bias of \mathcal{N} , for $\mathcal{N} = 0.66$ (top), 1.00 (middle), and 1.53 (bottom).

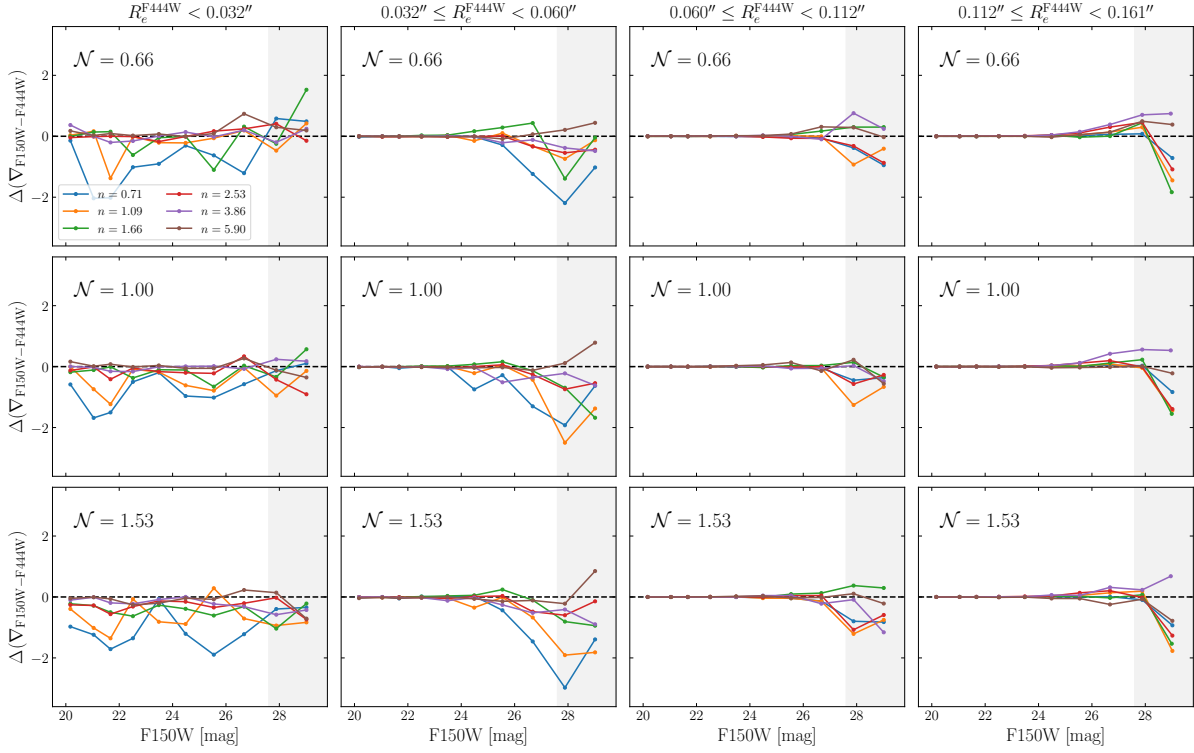


Figure B3. As in Figure B1, but for the bias of $\nabla_{F150W-F444W}$, for $\mathcal{N} = 0.66$ (top), 1.00 (middle), and 1.53 (bottom).

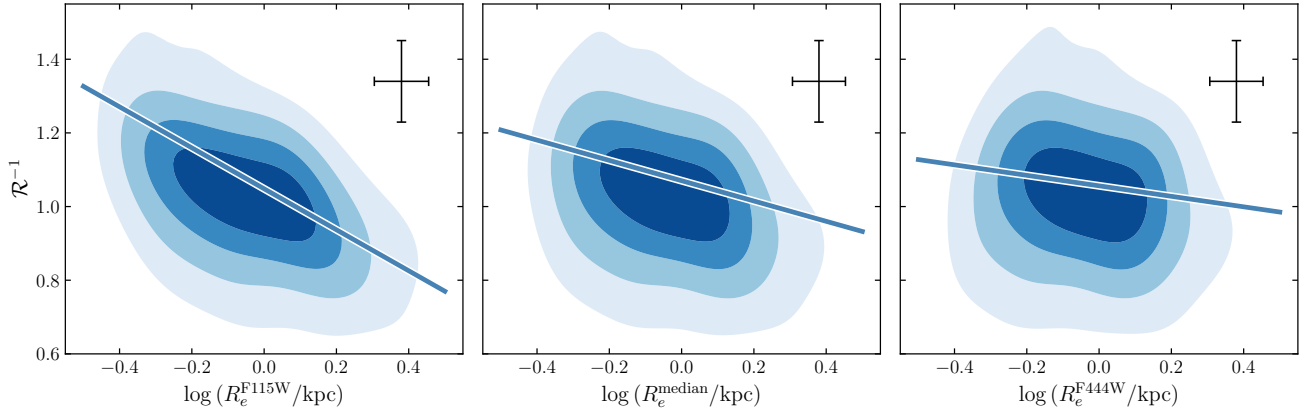


Figure C1. Dependence of the variation in effective radius \mathcal{R} on galaxy effective radius R_e measured in F115W (left), the median of different bands (middle), and F444W (right). The solid line gives the best-fit linear regression. The error bars indicate the median uncertainty of the data points. The blue-filled contour shows the density distribution of the data points, where the darker color signifies higher density.

REFERENCES

- Abdurro'uf, & Akiyama, M. 2018, *MNRAS*, 479, 5083
- Abdurro'uf, Coe, D., Jung, I., et al. 2023, *ApJ*, 945, 117
- Bagley, M. B., Finkelstein, S. L., Koekemoer, A. M., et al. 2023, *ApJL*, 946, L12
- Bagley, M. B., Pirzkal, N., Finkelstein, S. L., et al. 2024, *ApJL*, 965, L6
- Baker, W. M., Tacchella, S., Johnson, B. D., et al. 2024, *Nature Astronomy*
- Bradley, L., Sipócz, B., Robitaille, T., et al. 2024, *Astropy/Photutils: 1.12.0*, Zenodo
- Brammer, G. B., van Dokkum, P. G., & Coppi, P. 2008, *ApJ*, 686, 1503

- Cappellari, M., McDermid, R. M., Alatalo, K., et al. 2013, MNRAS, 432, 1862
- Carton, D., Brinchmann, J., Contini, T., et al. 2018, MNRAS, 478, 4293
- Casey, C. M., Kartaltepe, J. S., Drakos, N. E., et al. 2023, ApJ, 954, 31
- Cheng, C., Xu, C. K., Xie, L., et al. 2020, A&A, 633, A105
- Ciotti, L. 1991, A&A, 249, 99
- Dekel, A., Ginzburg, O., Jiang, F., et al. 2020, MNRAS, 493, 4126
- Duncan, K., Conselice, C. J., Mundy, C., et al. 2019, ApJ, 876, 110
- Eisenstein, D. J., Willott, C., Alberts, S., et al. 2024, ApJS, submitted (arXiv:2306.02465)
- Finkelstein, S. L., Bagley, M. B., Ferguson, H. C., et al. 2023, ApJL, 946, L13
- Frankel, N., Sanders, J., Rix, H.-W., Ting, Y.-S., & Ness, M. 2019, ApJ, 884, 99
- Fudamoto, Y., Oesch, P. A., Faisst, A., et al. 2020, A&A, 643, A4
- Giménez-Arteaga, C., Oesch, P. A., Brammer, G. B., et al. 2023, ApJ, 948, 126
- Graham, A. W., & Worley, C. C. 2008, MNRAS, 388, 1708
- Harikane, Y., Inoue, A. K., Ellis, R. S., et al. 2024, ApJ, submitted (arXiv:2406.18352)
- Harikane, Y., Zhang, Y., Nakajima, K., et al. 2023, ApJ, 959, 39
- Harris, C. R., Millman, K. J., van der Walt, S. J., et al. 2020, Nature, 585, 357
- Harvey, T., Conselice, C., Adams, N. J., et al. 2024, ApJ, submitted (arXiv:2403.03908)
- Hasheminia, M., Mosleh, M., Zahra Hosseini-ShahiSavandi, S., et al. 2024, ApJ, 975, 252
- Häußler, B., Bamford, S. P., Vika, M., et al. 2013, MNRAS, 430, 330
- Häußler, B., Vika, M., Bamford, S. P., et al. 2022, A&A, 664, A92
- Ho, L. C., Li, Z.-Y., Barth, A. J., Seigar, M. S., & Peng, C. Y. 2011, ApJS, 197, 21
- Hopkins, P. F., Bundy, K., Hernquist, L., et al. 2010, MNRAS, 401, 1099
- Hunter, J. D. 2007, Computing in Science & Engineering, 9, 90
- Ji, Z., Williams, C. C., Suess, K. A., et al. 2024, ApJ, submitted (arXiv:2401.00934)
- Jia, C., Wang, E., Wang, H., et al. 2024, ApJ, in press (arXiv:2411.07458)
- Kelvin, L. S., Driver, S. P., Robotham, A. S. G., et al. 2012, MNRAS, 421, 1007
- Kennedy, R., Bamford, S. P., Baldry, I., et al. 2015, MNRAS, 454, 806
- Kodra, D., Andrews, B. H., Newman, J. A., et al. 2023, ApJ, 942, 36
- Koekemoer, A. M., Faber, S. M., Ferguson, H. C., et al. 2011, ApJS, 197, 36,
- Kokorev, V., Caputi, K. I., Greene, J. E., et al. 2024, ApJ, 968, 38
- Kron, R. G. 1980, ApJS, 43, 305
- Labbé, I., Greene, J. E., Bezanson, R., et al. 2024, ApJ, submitted (arXiv:2306.07320)
- Lapiner, S., Dekel, A., Freundlich, J., et al. 2023, MNRAS, 522, 4515
- Larson, R. L., Hutchison, T. A., Bagley, M., et al. 2023, ApJ, 958, 141
- Li, Z.-Y., Ho, L. C., Barth, A. J., et al. 2011, ApJS, 197, 22
- Li, Y. A., Ho, L. C., Shangguan, J., et al. 2023, ApJS, 267, 17
- Li, Q., Narayanan, D., & Davé, R. 2019, MNRAS, 490, 1425
- Looser, T. J., D'Eugenio, F., Maiolino, R., et al. 2024, A&A, submitted (arXiv:2306.02470)
- Lyu, Y., Magnelli, B., Elbaz, D., et al. 2024, A&A, submitted (arXiv:2406.11571)
- Magnelli, B., Gómez-Guijarro, C., Elbaz, D., et al. 2023, A&A, 678, A83
- Marian, V., Ziegler, B., Kuchner, U., & Verdugo, M. 2018, A&A, 617, A34
- Matharu, J., Muzzin, A., Sarrouh, G., et al. 2023, ApJL, 949, L11
- Matharu, J., Nelson, E. J., Brammer, G., et al. 2024, A&A, submitted (arXiv:2404.17629)
- Miller, T. B., van Dokkum, P., & Mowla, L. 2023, ApJ, 945, 155
- Miller, T. B., Whitaker, K. E., Nelson, E. J., et al. 2022, ApJL, 941, L37
- Mitsuhashi, I., Tadaki, K.-i., Ikeda, R., et al. 2024, A&A, 690, A197
- Mo, H. J., Mao, S., & White, S. D. M. 1998, MNRAS, 295, 319
- Morishita, T., Stiavelli, M., Chary, R.-R., et al. 2024, ApJ, 963, 9
- Mosleh, M., Williams, R. J., Franx, M., et al. 2012, ApJ, 756, L12
- Muñoz-Mateos, J. C., Gil de Paz, A., Boissier, S., et al. 2007, ApJ, 658, 1006
- Nedkova, K. V., Häußler, B., Marchesini, D., et al. 2024a, MNRAS, 532, 3747
- Nedkova, K. V., Rafelski, M., Teplitz, H. I., et al. 2024b, ApJ, 970, 188

- Nelson, E. J., Tacchella, S., Diemer, B., et al. 2021, *MNRAS*, 508, 219
- Nelson, E. J., van Dokkum, P. G., Förster Schreiber, N. M., et al. 2016, *ApJ*, 828, 27
- Oke, J. B., & Gunn, J. E. 1983, *ApJ*, 266, 713
- Ono, Y., Harikane, Y., Ouchi, M., et al. 2024, *PASJ*, 76, 219
- Pandya, V., Zhang, H., Huertas-Company, M., et al. 2024, *ApJ*, 963, 54
- Peng, C. Y., Ho, L. C., Impey, C. D., & Rix, H.-W. 2002, *AJ*, 124, 266
- Peng, C. Y., Ho, L. C., Impey, C. D., & Rix, H.-W. 2010, *AJ*, 139, 2097
- Pérez, E., Cid Fernandes, R., González Delgado, R. M., et al. 2013, *ApJ*, 764, L1
- Pérez-Montero, E., García-Benito, R., Vílchez, J. M., et al. 2016, *A&A*, 595, A62
- Pezzulli, G., Fraternali, F., & Binney, J. 2017, *MNRAS*, stx029
- Planck Collaboration, Aghanim, N., Akrami, Y., et al. 2020, *A&A*, 641, A6
- Rieke, M. J., Kelly, D. M., Misselt, K., et al. 2023, *PASP*, 135, 028001
- Rigby, J., Perrin, M., McElwain, M., et al. 2023, *PASP*, 135, 048001
- Ryder, S. D., & Dopita, M. A. 1994, *ApJ*, 430, 142
- Schlafly, E. F., & Finkbeiner, D. P. 2011, *ApJ*, 737, 103
- Sérsic, J. L. 1968, *Atlas de Galaxias Australes* (Córdoba: Obs. Astron., Univ. Nac. Córdoba)
- Shen, S., Mo, H. J., White, S. D. M., et al. 2003, *MNRAS*, 343, 978
- Shibuya, T., Ouchi, M., & Harikane, Y. 2015, *ApJS*, 219, 15
- Simons, R. C., Papovich, C., Momcheva, I., et al. 2021, *ApJ*, 923, 203
- Skelton, R. E., Whitaker, K. E., Momcheva, I. G., et al. 2014, *ApJS*, 214, 24
- Stark, D. V., Tuttle, S., Tonnesen, S., et al. 2024, *ApJ*, 971, 116
- Stefanon, M., Yan, H., Mobasher, B., et al. 2017, *ApJS*, 229, 32
- Steinmetz, M. & Navarro, J. F. 2002, *NewA*, 7, 155
- Suess, K. A., Kriek, M., Price, S. H., & Barro, G. 2019, *ApJ*, 877, 103
- Sun, W., Ho, L. C., Zhuang, M.-Y., et al. 2024a, *ApJ*, 960, 104
- Sun, X., Wang, X., Ma, X., et al. 2024b, *ApJ*, submitted (arXiv:2409.09290)
- Tacchella, S., Carollo, C. M., Förster Schreiber, N. M., et al. 2018, *ApJ*, 859, 56
- Tacchella, S., Carollo, C. M., Renzini, A., et al. 2015, *Science*, 348, 314
- Tacchella, S., Dekel, A., Carollo, C. M., et al. 2016, *MNRAS*, 457, 2790
- The Astropy Collaboration, Robitaille, T. P., Tollerud, E. J., et al. 2013, *A&A*, 558, A33
- Tissera, P. B., Rosas-Guevara, Y., Sillero, E., et al. 2022, *MNRAS*, 511, 1667
- Tomassetti, M., Dekel, A., Mandelker, N., et al. 2016, *MNRAS*, 458, 4477
- Tonnesen, S., DeFelippis, D., & Tuttle, S. 2023, *ApJ*, 951, 16
- Treu, T., Calabro, A., Castellano, M., et al. 2023, *ApJL*, 942, L28
- Tripodi, R., D'Eugenio, F., Maiolino, R., et al. 2024, *A&A*, submitted (arXiv:2403.08431)
- Tuttle, S. E. & Tonnesen, S. 2020, *ApJ*, 889, 188
- Vader, J. P., Vigroux, L., Lachieze-Rey, M., & Souviron, J. 1988, *A&A*, 203, 217
- van der Wel, A., Chang, Y.-Y., Bell, E. F., et al. 2014a, *ApJL*, 792, L6
- van der Wel, A., Franx, M., van Dokkum, P. G., et al. 2014b, *ApJ*, 788, 28
- van der Wel, A., Martorano, M., Häußler, B., et al. 2024, *ApJ*, 960, 53
- van Dokkum, P. G., Leja, J., Nelson, E. J., et al. 2013, *ApJL*, 771, L35
- van Dokkum, P. G., Whitaker, K. E., Brammer, G., et al. 2010, *ApJ*, 709, 1018
- Vika, M., Bamford, S. P., Haeussler, B., et al. 2013, *MNRAS*, 435, 623
- Vika, M., Vulcani, B., Bamford, S. P., Häußler, B., & Rojas, A. L. 2015, *A&A*, 577, A97
- Virtanen, P., Gommers, R., Oliphant, T. E., et al. 2020, *Nature Methods*, 17, 261
- Vulcani, B., Bamford, S. P., Häußler, B., et al. 2014, *MNRAS*, 441, 1340
- Wang, B., Leja, J., Labbé, I., et al. 2024, *ApJS*, 270, 12
- Wang, W., Faber, S. M., Liu, F. S., et al. 2017, *MNRAS*, 469, 4063
- Ward, E. M., de la Vega, A., Mobasher, B., et al. 2024, *ApJ*, 962, 176
- White, S. D. M., & Frenk, C. S. 1991, *ApJ*, 379, 52
- Whitney, A., Ferreira, L., Conselice, C. J., & Duncan, K. 2021, *ApJ*, 919, 139
- Williams, R. J., Quadri, R. F., Franx, M., van Dokkum, P., & Labbé, I. 2009, *ApJ*, 691, 1879
- Yang, L., Morishita, T., Leethochawalit, N., et al. 2022, *ApJL*, 938, L17
- Zaritsky, D., Kennicutt, R. C., & Huchra, J. P. 1994, *ApJ*, 420, 87

Zhang, H., Primack, J. R., Faber, S. M., et al. 2019,
MNRAS, 484, 5170

Zhang, J., Wuyts, S., Cutler, S. E., et al. 2023, MNRAS,
524, 4128

Zhuang, M.-Y., & Ho, L. C. 2022, ApJ, 934, 130

Zhuang, M.-Y., Li, J., & Shen, Y. 2024, ApJ, 962, 93

Zhuang, M.-Y., & Shen, Y. 2024, ApJ, 962, 139

Zolotov, A., Dekel, A., Mandelker, N., et al. 2015, MNRAS,
450, 2327